Finite Elements in Analysis and Design 134 (2017) 82–91

Contents lists available at ScienceDirect

Finite Elements in Analysis and Design

journal homepage: www.elsevier.com/locate/finel

Austempering heat treatment of ductile iron: Computational simulation and experimental validation

A.D. Boccardo[a,b,*], P.M. Dardati[b], D.J. Celentano[c], L.A. Godoy[a,d]

[a] Instituto de Estudios Avanzados en Ingeniería y Tecnología, IDIT, CONICET-Universidad Nacional de Córdoba, Vélez Sarsfield 1611, Córdoba, Argentina
[b] Grupo de Investigación y Desarrollo en Mecánica Aplicada, GIDMA, Facultad Regional Córdoba, Universidad Tecnológica Nacional, Maestro M. Lopez esq. Cruz Roja Argentina, Córdoba, Argentina
[c] Department of Mechanical and Metallurgical Engineering, Research Center for Nanotechnology and Advanced Materials (CIEN-UC), Pontificia Universidad Católica de Chile, Vicuña Mackenna 4860, Santiago de Chile, Chile
[d] Facultad de Ciencias Exactas, Físicas y Naturales, Universidad Nacional de Córdoba, Vélez Sarsfield 1611, Córdoba, Argentina

ARTICLE INFO

Keywords:
Austempered Ductile Iron (ADI)
Finite element analysis
Experimental validation
Heat treatment simulation
Thermo-mechanical-metallurgical model

ABSTRACT

The *three-step* austempering heat treatment of ductile iron parts in this paper is simulated by employing a coupled thermo-mechanical-metallurgical model. The thermo-mechanical formulation is solved in the macro-scale using the finite element method to predict the evolution of temperatures and deformations in the whole part. The metallurgical model deals with phase transformations that occur during the heat treatment, which are analyzed in the microscale. For each phase transformation the microstructure features such as type, distribution, and shape and size of phases are considered employing representative volume elements. The performance of the proposed model is tested by simulating experimental heat treatments reported in the literature. By means of comparison with experimental results, the model proved to be able to predict correctly the evolutions of temperature and dimensional changes, the minimum austenitization and austempering times, and the final phase fractions. It is concluded that this model could be a useful computational tool in the design of austempered ductile iron parts as well as the austempering heat treatment process.

1. Introduction

Austempered Ductile Iron (ADI) is a metallic alloy of growing interest in industry because it allows to obtain high resistance parts at low production cost. ADI parts, which are mostly used by automotive and agricultural industries, are obtained by means of casting and heat treatment processes. At ambient temperature, the ADI microstructure is formed by graphite nodules embedded in a metallic matrix called ausferrite. The ausferrite is a microstructure constituent in which the phases are retained austenite and ferrite platelets. The features and amount of these phases are important because they modify the mechanical properties values of the material.

The classical austempering heat treatment, which has been reported in numerous publications, is commonly identified as *three-step* heat treatment [1,2] and its main features are shown in Fig. 1. In this process the austenitization stage first takes place in which the part is heated up and kept at the austenitizing temperature T_γ, this is between 850 °C and 950 °C, in order to transform the initial matrix, commonly ferritic-pearlitic, into one completely austenitic and with the appropriate carbon content [3,4]. Next, the part is suddenly cooled down and kept at the austempering temperature T_A, this is between 250 °C and 450 °C, to initiate the austempering process (austempering stage). Finally, the part is cooled down up to the ambient temperature T_{amb}. The extension of the first stage and second stage are called austenitization time (t_γ) and austempering time (t_A), respectively.

A set of heat treatment process parameters play a key role in the obtained ADI microstructure and consequently in the resulting mechanical properties; among them the austenitization and austempering temperatures, austenitization and austempering times, and the cooling rate when the part is cooled down from T_γ up to T_A are the most important. In several experimental investigations the adequate value of these parameters have been reported, but only for a small variety of parts size and shape, and ductile iron features (chemical composition, graphite nodule count, initial microstructure) [5–9]. Thus, the design of new ADI parts currently requires a number of experimental tests, with the consequence that there are heavy increases in cost and time every time a new development is attempted.

To reduce cost and time of new developments, computational models may be a way to improve designs without the need to perform trials in laboratory environments. This allows estimating appropriate

* Corresponding author at: Instituto de Estudios Avanzados en Ingeniería y Tecnología, IDIT, CONICET-Universidad Nacional de Córdoba, Vélez Sarsfield 1611, Córdoba, Argentina.
E-mail address: aboccardo@frc.utn.edu.ar (A.D. Boccardo).

http://dx.doi.org/10.1016/j.finel.2017.06.002
Received 22 March 2017; Received in revised form 29 May 2017; Accepted 16 June 2017

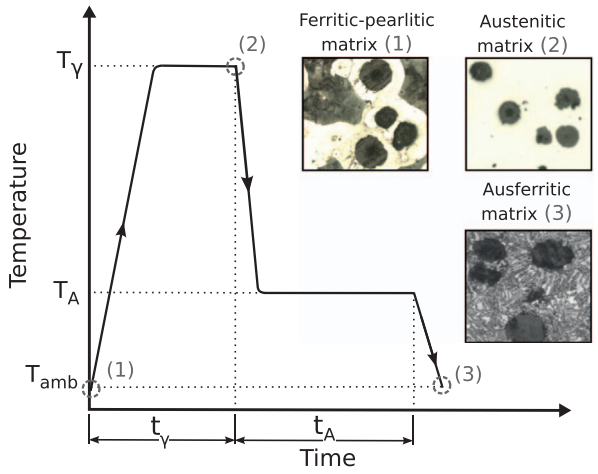

Fig. 1. *Three-step* austempering heat treatment.

values of heat treatment parameters by employing physical models that deal with the different phenomena that take place in the process. In the literature, several heat treatment models that consider thermal, mechanical and metallurgical phenomena are found for materials like steels [10–16]; however, regarding to the austempering heat treatment of ductile irons, most simulations are restricted to metallurgical aspects. For example Batra et al. [17] predicted the evolution of phases during the stable reverse eutectic transformation using a model that considers some microstructure features of the ductile iron such as graphite nodule count. Yescas et al. [4] proposed a model to predict the amount of austenite, ferrite platelets, and martensite at ambient temperature when the ausferritic transformation is completely developed. Thomson et al. [18] and Kapturkiewicz et al. [19] proposed different models to simulate the kinetics of the austempering transformation, whereas along the same line of thought, Boccardo et al. [20] considered the graphite nodule count and ferrite platelet size. A few models simultaneously consider the phenomena of different nature of the process in a coupled way. Kapturkiewicz et al. [21] predicted the evolutions of temperature and phases during the metastable reverse eutectic transformation using a thermo-metallurgical model that considers the microstructure features of the ductile iron such as the pearlite interlaminar spacing. Hepp et al. [22] simulated the heat treatment employing a thermo-metallurgical approach, in which the metallurgical model took into account phase transformations such as reverse eutectoid, eutectoid, and ausferritic. Boccardo et al. [23] proposed a thermo-mechanical-metallurgical approach considering the reverse eutectoid, ausferritic, and martensitic transformations. The two last mentioned models were the most complete found in the literature review to simulate the *three-step* process; however they have some limitations regarding the metallurgical model: In both models, the effect of graphite nodule size has been neglected in the ausferritic transformation even though the kinetics of this transformation is strongly modified by graphite nodule size, as reported by Fra's et al. [8]. Furthermore, the martensitic transformation model employ by Refs. [4,23] considers austenite with homogeneous carbon concentration even though the austenite, that will transform into martensite after ausferritic transformation, has no homogeneous carbon concentration during the ausferritic transformation due to the redistribution of carbon [24,25].

The aim of this work is to simulate the austempering heat treatment process of a ductile iron taking into account the thermal, mechanical, and metallurgical aspects of the problem. The formulation is defined within the context of the thermo-plasticity theory and takes into account large strain effects, volumetric deformations on account of thermal and phase changes, temperature-dependent material properties, and metallurgical evolution. The metallurgical model considers the reverse eutectoid, ausferritic, and martensitic transformations, which are modeled by deterministic representative volume elements, which account for some microstructure features that were not considered by the above mentioned works. The austempering heat treatment model is first presented (Section 2), followed by cases studied (Section 3) and their results and discussion (Section 4). Finally, conclusions are presented (Section 5).

2. Austempering heat treatment model

The proposed heat treatment model considers the thermal, mechanical, and metallurgical aspects of the problem. The thermal aspect deals with the evolution of the temperature in the part at macroscale. The mechanical aspect, also proposed at macroscale, handles the evolution of the deformation due to phase and temperature changes. Finally, the metallurgical aspect evaluates the evolution of phases at microscale level to consider the type, distribution, and shape and size of the phases that form the microstructure.

The thermal and mechanical models are solved by means of the finite element method, meanwhile the differential equations of the metallurgical model are solved, at each Gauss point of a finite element, by the implicit Euler method. In this paper a bidirectional coupling has been proposed between the thermal and the metallurgical models which allows to predict the evolution of phases as a function of the temperature and, in turn, the evolution of the temperature as a function of the phase evolution. On the other hand, unidirectional couplings have been proposed between the metallurgical and the mechanical, and the thermal and the mechanical models, in this way only the deformation evolution by phase and temperature changes are considered. The numerical solution at time $t + \Delta t$ is calculated, taking into account the couplings mentioned above, by means of the algorithms schematically illustrated in the Fig. 2.

2.1. Thermo-mechanical formulation

The thermo-mechanical formulation used in this paper is based on previous works [23,26,27]. The local governing equations describing the evolution of a quasi-steady process are expressed by the continuity equation (Eq. (1)), the motion equation (Eq. (2)), and the energy balance equation (Eq. (3)) written in a Lagrangian description, and are valid in $\Omega \times Y$, where Ω is the spatial configuration of a body and Y denotes the time interval of interest with time $t \in Y$.

$$\rho J = \rho_0 \tag{1}$$

$$\nabla \boldsymbol{\sigma} = 0 \tag{2}$$

$$\rho c \dot{T} = \nabla \cdot (\mathbf{k} \nabla T) + \dot{Q} \tag{3}$$

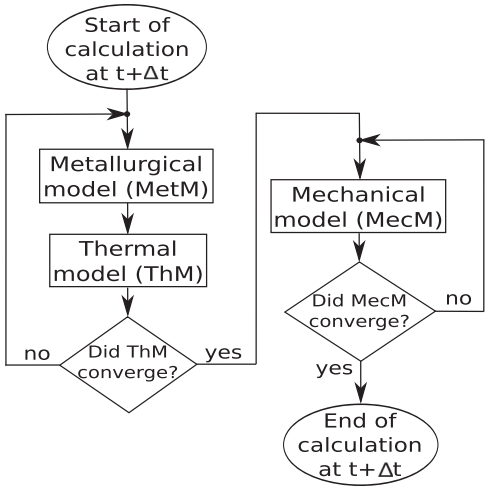

Fig. 2. Resolution scheme of the austempering heat treatment model at time $t + \Delta t$.

where ρ is the density, J is the determinant of the deformation gradient tensor $\mathbf{F}$, $\boldsymbol{\sigma}$ is the Cauchy stress tensor, c is the tangent specific heat capacity, Q is the heat generated due to phase changes, $\mathbf{k}$ is the isotropic conductivity tensor defined as $\mathbf{k} = k\mathbf{1}$, where k is the conductivity coefficient and $\mathbf{1}$ is the unit tensor, and T is the temperature. In these equations ∇ is the spatial gradient operator, the dot on top of a variable indicates time derivative, and the subscript 0 applied to a variable denotes its value at the initial configuration Ω_0. The material parameters c and k are temperature-dependent.

The rate of the heat generation due to phase change is calculated as:

$$\dot{Q} = \rho(L_{\alpha\to\gamma}\dot{f}_{\gamma_s} + L_{p\to\gamma}\dot{f}_{\gamma_m} + L_{\gamma\to\alpha}\dot{f}_{\alpha p}) \tag{4}$$

where $L_{\alpha\to\gamma}$, $L_{p\to\gamma}$ and $L_{\gamma\to\alpha}$ are the latent heats of stable reverse eutectoid, metastable reverse eutectoid, and ausferritic transformations, respectively. The volume fractions f_{γ_s}, f_{γ_m}, and $f_{\alpha p}$ correspond to stable and metastable austenite, and ferrite platelets, respectively.

The boundary condition imposed at the casting/environment interface respond to a Newton type law (Eq. (5)), which is valid in Γ_qxY, where Γ_q is the Ω contouring in which the condition is applied.

$$q_{conv} = -h(T - T_{env}) \tag{5}$$

where q_{conv} is the normal heat flux, h is the heat transfer coefficient at interface, and T and T_{env} are the temperatures at both sides of the interface.

2.2. Elasto-plastic constitutive model

The stress-strain law and the plastic evolution equations are defined within the context of the associate rate-independent thermo-plasticity theory. The relationship between the stress $\boldsymbol{\sigma}$ and total strain $\mathbf{e}$ is given by the secant constitutive law defined as:

$$\boldsymbol{\sigma} = \mathbf{C}\colon(\mathbf{e} - \mathbf{e}^p - \mathbf{e}^v) \tag{6}$$

where $\mathbf{C}$ is the temperature-dependent isotropic elastic constitutive tensor, $\mathbf{e} = 1/2(\mathbf{1} - \mathbf{F}^{-T}\mathbf{F}^{-1})$ is the Almansi strain tensor, $\mathbf{e}^p$ is the plastic Almansi strain tensor, and $\mathbf{e}^v$ is the Almansi strain tensor associated to a volume expansion or contraction due to temperature and phase changes.

The evolution of $\mathbf{e}^p$ is given by:

$$L_v(\mathbf{e}^p) = \dot{\lambda}(\partial F/\partial\sigma) \tag{7}$$

in which L_v is the Lie derivative, $\dot{\lambda}$ is the plastic consistency parameter computed according to classical concepts of the plasticity theory, and $F = F(\boldsymbol{\sigma}, \bar{e}^p, T)$ is the yield function governing the plastic behavior of the solid, such that no plastic evolutions occur when $F < 0$. A von Mises yield function is adopted:

$$F = (3J_2)^{1/2} - (C_{y_0} + C_h) \tag{8}$$

where $\sigma_{eq} = (3J_2)^{1/2}$ is the equivalent or von Mises stress, J_2 is the second invariant of the deviatoric part of $\boldsymbol{\sigma}$, C_{y_0} is the yield strength defining the initial elastic boundary of the material, and C_h is the isotropic plastic hardening function. In general C_{y_0} decreases with temperature and, hence, it accounts for the thermal softening phenomenon, which is an important effect to be considered in heat treatment processes where materials undergo large temperature variations. The function C_h depends on the effective plastic deformation related to the isotropic strain hardening effect $\bar{e}^p$ in the form:

$$C_h = A^p(\bar{e}^p)^{n^p} \tag{9}$$

where

$$\dot{\bar{e}}^p = -\dot{\lambda}(\partial F/\partial C_h) \tag{10}$$

In Eq. (9) A^p is the strength index and n^p is the strain hardening exponent.

The strain tensor $\mathbf{e}^v$ is given by:

$$\mathbf{e}^v = \frac{1}{2}[1 - (1 - a_v)^{2/3}]\mathbf{1} \tag{11}$$

where a_v is the secant volumetric deformation. The definition of a_v takes into account the volumetric deformation due to temperature and phase changes. Following Ref. [28], the function a_v is evaluated as:

$$a_v = \frac{\rho_0^{mic}}{\rho^{mic}} - 1 \tag{12}$$

where ρ^{mic} is the microstructure density which is calculated in the form:

$$\rho^{mic} = \sum f_{ph}\rho_{ph} \tag{13}$$

where f_{ph} and ρ_{ph} are the volume fraction and density of the microconstituents, respectively, indicated by the subscript ph which represents to graphite (Gr), ferrite (α), ferrite platelets (αp), pearlite (p), block (m_b) and halo (m_h) of martensite, and film (γ_f), block (γ_b), and halo (γ_h) of austenite. Because pearlite is formed by ferrite and cementite, its density is computed as:

$$\rho_p = f_{\theta/p}\rho_\theta + (1 - f_{\theta/p})\rho_\alpha \tag{14}$$

where ρ_θ is the density of cementite and $f_{\theta/p}$ is the volume fraction of cementite in the pearlite colonies which is calculated as:

$$f_{\theta/p} = \frac{c_{Pear} - c_{\alpha/\theta}}{c_\theta - c_{\alpha/\theta}} \tag{15}$$

where c_{Pear} is the carbon concentration of pearlite, $c_{\alpha/\theta}$ is the equilibrium carbon concentration of ferrite at ferrite-cementite interface, and c_θ is the carbon concentration of cementite, and they are calculated as in Ref. [23].

The ferrite, austenite, and cementite densities are computed as described in Ref. [29], and the graphite density is computed as in Ref. [23]. The volume fraction of all the phases employed in Eq. (13) are computed with the metallurgical model below described.

2.3. Metallurgical model

The metallurgical model simulates the phase transformations that occur through the *three-step* heat treatment. The considered transformations are stable (TEI_s) and metastable (TEI_m) reverse eutectoide, ausferritic (TA), and martensitic (TM). Moreover the carbon homogenization in austenite (HA), at the austenitization temperature, is taken into account. These transformations occur in specific stages of the heat treatment and their development depend on the values of temperature, temperature rate, and phase fraction. Fig. 3 shows the algorithms of the metallurgical model that allows to obtain the final microstructure, where $T_{EI_S S}$, $T_{EI_M S}$, T_{AS}, and T_{MS} represent the temperature at which the transformations TEI_s, TEI_m, TA, and TM start. The temperatures $T_{EI_S S}$ and $T_{EI_M S}$ are calculated using the equations

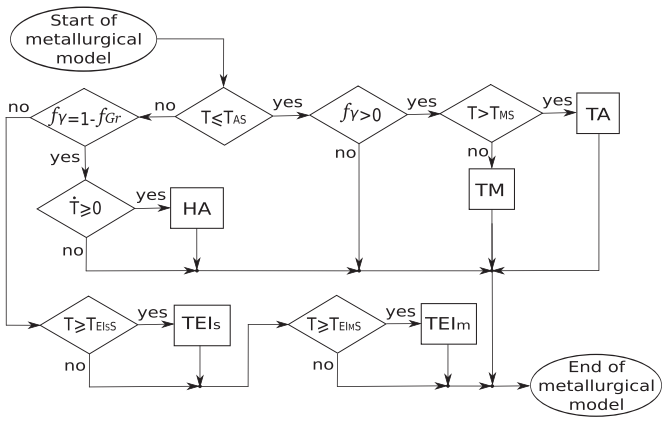

Fig. 3. Resolution scheme of the metallurgical model.

proposed by Ref. [30], while T_{AS} and T_{MS} are calculated using the equations proposed by Refs. [31] and [32], respectively.

For each transformation, the microstructure of the material is described by a representative volume element (RVE), in which the temperature is assumed uniform. These RVEs allow to model the phase change by considering the type, distribution, and shape and size of the phases that form the microstructure of the ductile iron during the different stages of the heat treatment. The models for TEI_s and TEI_m are described in Section 2.3.1, while those for *HA*, *TA*, and *TM* are described in Sections 2.3.2, 2.3.3 and 2.3.4, respectively.

2.3.1. Reverse eutectoid transformation

At the beginning of the simulation, the initial microstructure is formed by graphite nodules, ferrite halos, and pearlite colonies, all of these having diverse sizes. The ferrite halos are transformed into austenite (γ_s) by means of the stable reverse eutectoid transformation. In this transformation, for each set of equal size graphite nodules, the employed spherical representative volume element RVE_{s_i} is formed by a graphite nodule surrounded by a ferrite shell, see Fig. 4.

The model considers that an instantaneous austenite shell, of radius 1% larger than the graphite nodule, occurs at graphite-ferrite interface. The growth mechanism is governed by long range carbon diffusion. The graphite and austenite radii growth rates, for each set of equal size graphite nodules, are computed through the carbon mass balance condition at the mobile graphite-austenite and austenite-ferrite interfaces, together with the steady state carbon diffusion and carbon mass conservation in the RVE_{s_i}. The radii growth $\dot{r_{Gr_i}}$ and $\dot{r_{\gamma_i}}$ are evaluated employing the equations of Ref. [23]. The graphite, ferrite, and austenite volume fractions are calculated as:

$$f_{Gr} = \frac{4\pi}{3} \sum_{i=1}^{nsetsg} N_{set_i} r_{Gr_i}^3 \tag{16}$$

$$f_{\gamma_s} = \frac{4\pi}{3} \sum_{i=1}^{nsetsg} N_{set_i} (r_{\gamma_i}^3 - r_{Gr_i}^3) \tag{17}$$

$$f_{\alpha} = \frac{4\pi}{3} \sum_{i=1}^{nsetsg} N_{set_i} (r_{\alpha_i}^3 - r_{\gamma_i}^3) \tag{18}$$

where r_{Gr_i} is the radius of graphite nodule, r_{γ_i} is the radius of austenite shell, and r_{α_i} is the size of RVE_{s_i}. In addition, N_{set_i} is the number of nodules per unit volume, all of them of a set *i*, such that *nsetsg* is the number of sets. The initial radius of graphite nodule is $r_{Gr_{i_o}} = [(3 f_{set_i} f_{Gr_o})/(4\pi N_{set_i})]^{1/3}$, where f_{set_i} is the normalized initial graphite volume fraction with respect to f_{Gr_o}. The size of RVE_{s_i} is calculated as $r_{\alpha_i} = r_{Gr_{i_0}}(1 + f_{\alpha 0}/f_{Gr0})^{1/3}$.

When the initial graphite and ferrite volume fractions are high enough, there are contacts between neighbouring shells of austenite which are growing, therefore the austenite growth rate decreases. This phenomenon is taken into account with a coefficient called GI_{EI}, with $GI_{EI} < 1$, which reduces $\dot{r_{\gamma_i}}$ when the shells begin to be in contact:

$$GI_{EI} = \left[\frac{1 - (f_{Gr} + f_{\gamma_s})}{1 - f_{con}} \right]^{2/3} \tag{19}$$

where f_{con} is the sum of f_{Gr} and f_{γ_s} when the neighbouring shells of austenite begin to be in contact and it is set to $f_{con} = 0.5$ as in Ref. [23].

On the other hand, the pearlite is transformed into austenite (γ_m) by means of the metastable reverse eutectoid transformation. The pearlite colonies are classified in sets of equal interlaminar spacing. Set *j* is formed by all pearlite colonies with an interlaminar spacing size ips_j. In this transformation, for each set of pearlite colonies the employed unidimensional representative volume element RVE_{m_j} is formed by a half layer of cementite and a half layer of ferrite as is shown in Fig. 5.

The model considers that an instantaneous austenite layer, of thickness equal to 1% of the cementite layer, occurs at cementite-ferrite interface. The growth mechanism is governed by long range carbon diffusion. The carbon mass balance condition at the mobile cementite-austenite and austenite-ferrite interfaces is considered, together with steady state carbon diffusion and carbon mass conservation in RVE_{m_j}. The interfaces growth $\dot{x_{\theta_j}}$ and $\dot{x_{\gamma_j}}$ are evaluated employing the equations of Ref. [23]. The pearlite and austenite volume fractions are calculated as:

$$f_p = \sum_{j=1}^{nsetsc} f_{p_j} \left[1 - \frac{\left(x_{\gamma_j} - x_{\theta_j} \right)}{x_{\alpha_j}} \right] \tag{20}$$

$$f_{\gamma_m} = \sum_{j=1}^{nsetsc} f_{p_j} \frac{\left(x_{\gamma_j} - x_{\theta_j} \right)}{x_{\alpha_j}} \tag{21}$$

where x_{θ_j} and x_{γ_j} are the coordinates of cementite-austenite and austenite-ferrite interfaces respectively, and x_{α_j} is the size of RVE_{m_j}. Further, f_{p_j} is the pearlite volume fraction, all of them for a set *j*, such that *nsetsc* is the number of sets. The size of RVE_{m_j} is calculated as $x_{\alpha_j} = ips_j/2$ and $x_{\theta_{j0}} = x_{\alpha_j} f_{\theta/p}$.

The total austenite volume fraction resulting of the reverse eutectoid transformation is evaluated with the following equation:

$$f_{\gamma} = f_{\gamma_h} = f_{\gamma_s} + f_{\gamma_m} \tag{22}$$

2.3.2. Carbon homogenization in austenite

After the end of both stable and metastable reverse eutectoid transformations, the microstructure of the ductile iron is formed by

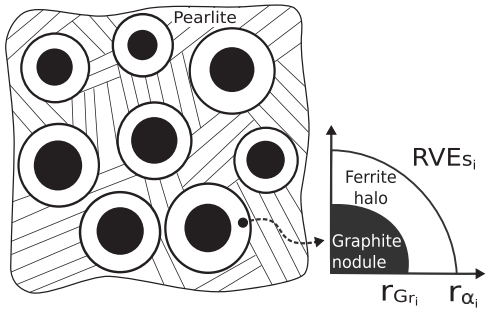

Fig. 4. Representative volume element RVE_{s_i} employed to model the stable reverse eutectoid transformation.

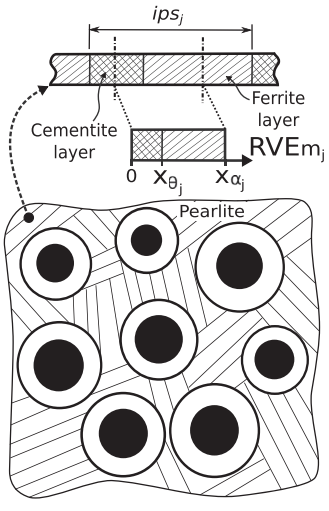

Fig. 5. Representative volume element RVE_{m_j} employed to model the metastable reverse eutectoid transformation.

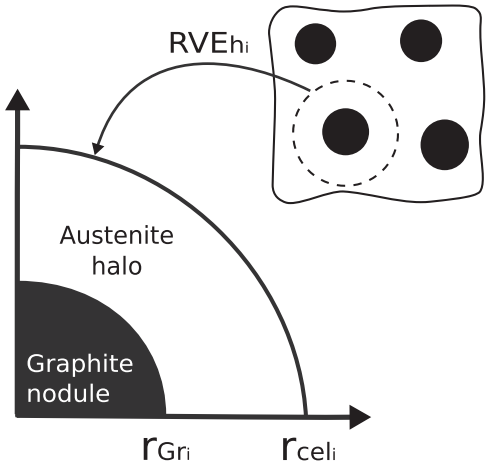

Fig. 6. Representative volume element RVE_{h_i} proposed to model the carbon homogenization in austenite.

graphite nodules and austenite. The austenite carbon concentration, in equilibrium with graphite, increases as the austenitization temperature increases. This equilibrium carbon concentration is reached by means of carbon diffusion from graphite nodules to austenite through graphite-austenite interface.

By proposing a RVE_{h_i} as is shown in Fig. 6 and taking into account the graphite nodule size, the graphite and austenite volume fractions became:

$$f_{Gr} = \frac{4\pi}{3}\sum_{i=1}^{nsetsg} N_{set_i} r_{Gri}^3 \tag{23}$$

$$f_\gamma = f_{\gamma_h} = \frac{4\pi}{3}\sum_{i=1}^{nsetsg} N_{set_i}(r_{cel_i}^3 - r_{Gr_i}^3) \tag{24}$$

where $r_{cel_i} = [(3f_{set_i})/(4\pi N_{set_i})]^{1/3}$ is the size of RVE_{h_i}.

The carbon mass balance condition at the mobile graphite-austenite interface is considered, together with steady state carbon diffusion and carbon mass conservation in RVE_{h_i}. The radius growth $\dot{r_{Gr_i}}$ is calculated in the same way as it was obtained for the stable reverse eutectoid transformation.

2.3.3. Ausferritic transformation

During the ausferritic transformation a fraction of austenite transforms into ferrite platelets. In this work the model proposed by Boccardo et al. [20] is used. This model considers a continuously nucleation of ferrite platelets on both graphite surface and tips of the existing ferrite platelets, and they grow by means of a displacive mechanism. This transformation occurs if austenite carbon concentration is less than $C_{\gamma_{T_0'}}$, phenomenon known as incomplete reaction. The spherical RVE_{A_i} employ to this transformation is observed in Fig. 7, which considers three regions of austenite with different carbon contents: (1) austenite film that forms part of the sheaves, (2) austenite block that is placed between the sheaves, and (3) austenite halo, all of them with different carbon content during the development of the mentioned transformation. The austenite film, austenite block, and ferrite subunits form a microconstituent called ausferrite.

It is assumed that the graphite fraction remains constant, while volume fractions of ausferrite, ferrite platelets, austenite film, austenite block, and austenite halo, are evaluated as:

$$f_{Ausf} = \frac{4\pi}{3}\sum_{i=1}^{nsetsg} N_{set_i}(r_{A_i}^3 - r_{Gr_i}^3) \tag{25}$$

$$f_{ap} = \frac{4\pi}{3}\sum_{i=1}^{nsetsg} f_{ap_i} N_{set_i} r_{cel_i}^3 \tag{26}$$

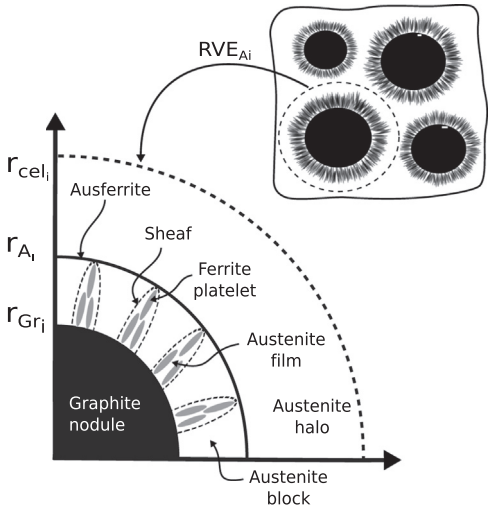

Fig. 7. Representative volume element RVE_{A_i} employ to model the ausferritic transformation.

$$f_{\gamma_f} = \frac{4\pi}{3} x_{\gamma f/ap} \sum_{i=1}^{nsetsg} f_{ap_i} N_{set_i} r_{cel_i}^3 \tag{27}$$

$$f_{\gamma_b} = \frac{4\pi}{3}\sum_{i=1}^{nsetsg} [N_{set_i}(r_{A_i}^3 - r_{Gr_i}^3) - f_{ap_i} N_{set_i}(1 + x_{\gamma f/ap}) r_{cel_i}^3] \tag{28}$$

$$f_{\gamma_h} = \frac{4\pi}{3}\sum_{i=1}^{nsetsg} N_{set_i}(r_{cel_i}^3 - r_{A_i}^3) \tag{29}$$

where r_{A_i} is the radius of ausferrite, f_{ap_i} is the volume fraction of ferrite platelet with respect to the RVE_{A_i} volume, all of them of a graphite nodule set i. Moreover $x_{\gamma f/ap} = 0.12$ is the ratio between the volume fractions of austenite film and ferrite subunit within a sheaf. The radius and fraction growths $\dot{r_{A_i}}$ and $\dot{f_{ap_i}}$, respectively, are evaluated employing the equations of Ref. [20].

When the graphite and ausferrite volume fractions are high enough, there are contacts between neighbouring shells of ausferrite which are growing, therefore the ausferrite growth rate decreases. This phenomenon is taken into account with a coefficient called GI_A, with $GI_A < 1$, which reduces $\dot{r_{A_i}}$ when the shells begin to be in contact:

$$GI_A = \left[\frac{1 - (f_{Gr} + f_{Ausf})}{1 - f_{con}}\right]^{2/3} \tag{30}$$

where f_{con} is the sum of f_{Gr} and f_{Ausf} when the neighbouring shells of ausferrite begin to be in contact and it is set to $f_{con} = 0.5$ as in Ref. [20].

The total austenite volume fraction is calculated as:

$$f_\gamma = f_{\gamma_f} + f_{\gamma_b} + f_{\gamma_h} \tag{31}$$

2.3.4. Martensitic transformation

The model proposed in this work allows predicting the amount of martensite formed within austenite film, austenite block, and austenite halo employing the model of Ref. [4] for each austenite region, as is illustrated in Fig. 8. Austenite film is retained at ambient temperature due to its high carbon concentration [24], whereas austenite block and halo are able to transform into martensite if the ausferritic transformation has not been developed completely. When the ausferritic transformation is completed, there is no austenite halo and the carbon concentration of austenite block is equal to the carbon concentration of austenite film, hence the martensitic transformation does not occur.

During the martensitic transformation it is assumed that graphite volume fraction remains constant, while the volume fractions of martensite (f_m) and austenite (f_γ) are calculated as:

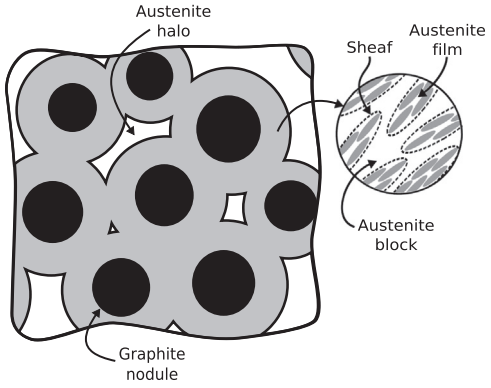

Fig. 8. Schematic representation of ADI microstructure after the ausferritic transformation took place.

$$f_m = f_{(\gamma_b \to m)} f_{\gamma_b}^o + f_{(\gamma_h \to m)} f_{\gamma_h}^o \tag{32}$$

$$f_\gamma = f_{\gamma_b}^o + f_{\gamma_h}^o - f_m \tag{33}$$

where $f_{\gamma_b}^o$ and $f_{\gamma_h}^o$ are the volume fractions of austenite block and halo, respectively, when the martensitic transformation starts. Furthermore, $f_{(\gamma_b \to m)}$ and $f_{(\gamma_h \to m)}$ are the volume fractions of austenite block and halo, respectively, that transform into martensite, which are calculated by means of the Khan and Bhadeshia model [33]:

$$\frac{-\ln\left(1 - f_{(\gamma_j \to m)}\right)}{f_{(\gamma_j \to m)}} = 1 + c_2 (T_{MSj} - T) \tag{34}$$

where c_2 is a fitted constant and $j = b, h$.

The proposed formulation was implemented into an in-house special purpose finite element code which has been extensively validated in previous engineering applications (see, for example, Refs. [23,26,27,34]). Assuming standard spatial interpolations for the displacement and temperature fields and following the typical procedures within the finite element context [35], the global discretized thermomechanical equations (also including microstructural effects) are solved using a staggered scheme based on an improved isothermal split. Moreover, the local evolution equations of the elastoplastic constitutive model are integrated in this work using an implicit radial return mapping algorithm written in the spatial configuration [36]. The equilibrium equation is solved by considering the continuum tangent elastoplastic constitutive tensor together with the B-bar technique to handle the incompressible character of the von Mises plastic flow. Further details of the full discretized formulation can be found elsewhere [26].

3. Cases of study

The model was tested by simulating experimental austempering heat treatments reported in the literature. In order to verify different aspects of the model two type of experiments, here identified as HT1 and HT2, were simulated.

In HT1 cylindrical samples of different dimensions are subjected to an austempering stage which is characterized for a complete development of the ausferritic transformation. The features of the different initial microstructures and chemical composition are shown in Table 1. The graphite nodule count per unit of area was transformed to graphite nodule count per unit of volume using the equation of Ref. [20]. These samples are treated employing the austenitization and austempering temperatures and times shown in Table 2.

In HT2 cuboid samples of 10 mm × 10 mm × 55 mm are subjected to different austempering time, consequently the final microstructure is able to contain martensite. The graphite nodule count, initial volume fractions, and chemical composition of the material are shown in Table 3. The austenitization and austempering temperatures are $T_\gamma = 900°C$ and $T_A = 330°C$, and the austenitization time is $t_\gamma = 60$ min, while the austempering time for each test is shown in Table 4.

Due to the symmetry of the cylindrical specimens a geometry corresponding to 1/2 sample was discretized using 600 linear axisymmetric elements of four nodes (6 × 100 elements), as shown in Fig. 9a. The mechanical boundary condition are applied in edges 1 and 2 (normal displacement equal to zero). The thermal boundary conditions are normal heat flux equal to zero in edges 1 and 2, and convection in edges 3 and 4. For the cuboid specimens there are three planes of symmetry, as shown in Fig. 9b, therefore the domain investigated reduces to 1/8 of the sample. This geometry was discretized using 540 linear hexahedral elements of 8 nodes (6 × 6 × 15 elements). The mechanical boundary condition are applied in surfaces 1, 2, and 3 (normal displacement equal to zero). The thermal boundary conditions are normal heat flux equal to zero in surfaces 1, 2, and 3, and convection in surfaces 4, 5, and 6. The number of elements for both geometries were obtained by means of a convergence study.

The mechanical and thermal properties for both chemical composi-

Table 1
Initial microstructure and chemical composition for HT1 [8,23,37].

Material	Graphite nodule count [nod/mm^2]	f_{Gr_0}	f_{α_0}	f_{p_0}
M1	140	0.11	0.42	0.47
M2	330	0.12	0.78	0.1
M3	840	0.11	0.46	0.43
M4	1992	0.1	0.1	0.8

Chemical composition DI1
3.70C-2.65Si-0.1Mn-0.02P-0.01S-0.04Mg

Table 2
Heat treatment parameters for HT1 [8,23,37].

Test	Material	Dimension [mm]	T_γ [°C]	T_A [°C]	t_γ [min]	t_A [min]
NC1	M1	ϕ2.5 × 40	900	400	40	33
NC2	M2	ϕ1.5 × 20	920	400	30	33
NC3	M3	ϕ2.5 × 40	900	400	40	33
NC4T1	M4	ϕ1.5 × 20	920	400	30	33
T2	M4	ϕ1.5 × 20	920	350	30	33
T3	M4	ϕ1.5 × 20	920	300	30	33

Table 3
Initial microstructure and chemical composition for HT2 [6].

Graphite nodule count [nod/mm^2]	f_{Gr_0}	f_{α_0}	f_{p_0}
250	0.09	0.045	0.865

Chemical composition DI2
3.48C-2.028Si-0.22Mn-0.05Cr-0.016Ni-0.6Cu-0.04Ti-0.03Mo-0.0079Sn-0.012V-0.02Al

Table 4
Austempering time for HT2 [6].

Test	t_A [min]
AT1	5
AT2	15
AT3	30
AT4	60
AT5	75
AT6	90
AT7	120
AT8	150

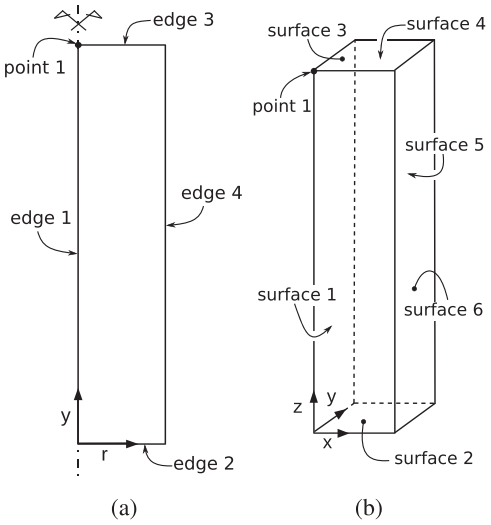

Fig. 9. Modeled geometry, and mechanical and thermal boundary conditions of (a) cylindrical and (b) cuboid samples.

Table 5
Mechanical properties of nodular cast iron [34].

Temperature [°C]	Young's modulus [MPa]	Yield strength [MPa]
20	163,471	260
100	163,113	255
200	160,174	250
300	151,650	230
400	135,276	210
500	110,898	135
600	81,386	60
700	52,021	50
720	46,668	48
750	44,267	45
770	43,788	42
800	44,356	40
830	45,935	37
850	42,935	35
900	35,435	30
1000	28,435	20
Poisson's ratio	$\nu = 0.33$	
Hardening parameters	$A^p = 300$ MPa	$n^p = 0.22$

Table 6
Thermal properties of nodular cast iron [21,34,38].

Temperature [°C]	Conductivity [W/(m °C)]	Specific heat [J/(kg °C)]
20	44.1	500
280	44.1	612
420	40.9	672
560	37.1	732
700	33.6	750
840	28.1	758
980	22.5	786
ρ_0[kg/m^3]	7000	
Latent heat [J/kg]	$L_{p\to\gamma} = 1.28x10^4$ $L_{\gamma\to\alpha} = 5.8x10^4$	$L_{\alpha\to\gamma} = 5.8x10^4$

tion are shown in Tables 5 and 6, respectively. The sample/environment heat transfer coefficient was fitted from experimental data. The average heat transfer coefficient is $h = 70$ W/(m^{2}K) during all the heating up and the cooling down from T_A up to T_{amb}, whereas $h = 400$ W/(m^{2}K) during the cooling down from T_γ up to T_A. In the initial microstructures, the graphite nodules and pearlite colonies were grouped in one set, i.e. *nsetsg* = 1 and *nsetsc* = 1. In this work a pearlite

Table 7
Fitted constants of the ausferritic transformation model.

Ductile iron	k_1	k_2 [J/mol]
DI1	$1.33x10^{15}$	$4.7x10^3$
DI2	$8x10^{15}$	$4.7x10^3$

with coarse interlaminar spacing $ips_1 = 0.5 \times 10^{-5}$ m was assumed. The constants of the ausferritic transformation model were fitted for both chemical composition, and their values are shown in Table 7. The constant of the martensitic transformation was also fitted and its value is $c_2 = 0.006$.

4. Results and discussion

In this work the heat treatment of two different small samples were treated using the described model. Some output in terms of temperature and dimensional change evolutions, phase fraction at the end of the heat treatment, minimum required time of the austenitization stage to obtain an austenitic matrix with homogeneous carbon content at austenitizing temperature (MRT_γ), and minimum required time of the austempering stage to complete the ausferritic transformation (MRT_A) are computed and compared with experimental results presented in Refs. [6,8,23].

The Fig. 10a shows the computed evolutions of temperature and dimensional change at point 1 for HT1. Moreover, the corresponding experimental measurements are also included in this figure. The dimensional change was defined as $d.\,c. = \Delta l/l_o$, were l_o is the initial length of the sample and Δl is its length change. As can be seen, the computed evolution of the temperature is in good agreement with experimental result. Besides, the dimensional change is well represented, that means expansion during the austenitization stage and contraction followed by expansion during the austempering stage. The calculated expansion during the austempering stage is smaller than the experimental one, but they have the same trend stating that the kinetics of the ausferritic transformation is correctly represented. The temperature and deformation evolutions at point 1 for HT2 is shown in Fig. 10b. The temperature curve shows clearly the thermal cycle and the dimensional change curve evidences the effects of reverse eutectoid, ausferritic, and martensitic transformations in regions A, B, and C, respectively.

In Figs. 11a and b the computed volume fraction of ferrite platelets, at the end of the heat treatment, is shown for cylindrical and cuboid samples, respectively. It can be observed that this fraction is almost homogeneous throughout the parts. It occurred because a similar temperature evolution was obtained in different points of each sample due to its small dimensions.

The computed volume fractions of graphite, austenite, ferrite platelets, and martensite through the heat treatment, for HT2, are shown in Fig. 12. The graphite volume fraction remained constant after the austenitization stage. Austenite volume fraction increased due to reverse eutectoide transformation, and decreased because it was consumed in both ausferritic and martensitic transformations. The martensitic transformation started because the ausferritic transformation was developed for a short time.

In Fig. 13 the time MRT_γ for HT1 is presented. The numerical results are in good agreement with experimental ones. By comparison between tests NC1 and NC3, which have coupons of same dimension and the metallic matrices are almost the same, could be observed the influence of the variation of the graphite nodule count. When the graphite nodule count increased from 140 to 840 nod/mm^2, MRT_γ decreased; the same behavior was observed by Frás et al. [8]. This occurs because the distance between neighbor graphite nodules decreases, therefore the carbon needs to diffuse a short distance. The obtained results indicate that the model allows predicting the mentioned time by taking into account the microstructure features.

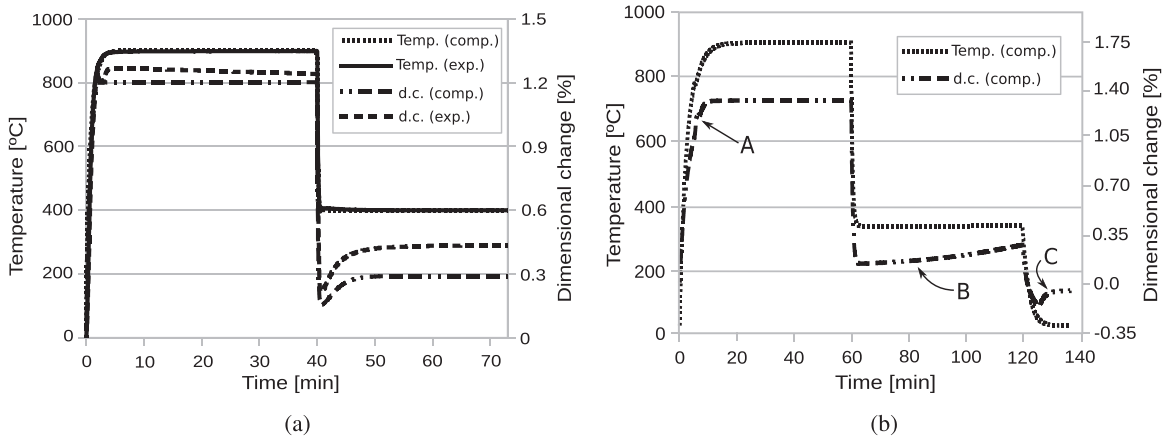

Fig. 10. Evolutions of temperature and dimensional change during the heat treatment of (a) cylindrical (test NC3) and (b) cuboid (test AT4) samples.

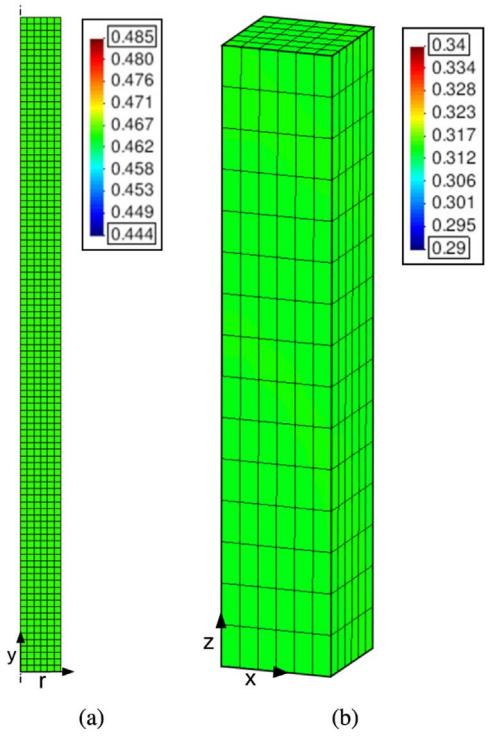

Fig. 11. Computed volume fraction of ferrite platelets at the end of the heat treatment for (a) cylindrical (test NC3) and (b) cuboid (test AT4) samples.

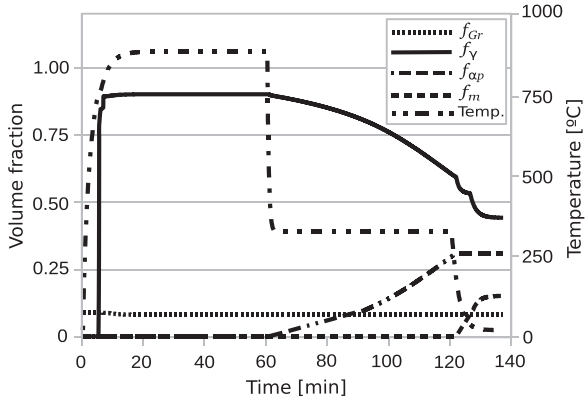

Fig. 12. Evolutions of phase fraction and temperature at point 1 for HT2 (test AT4).

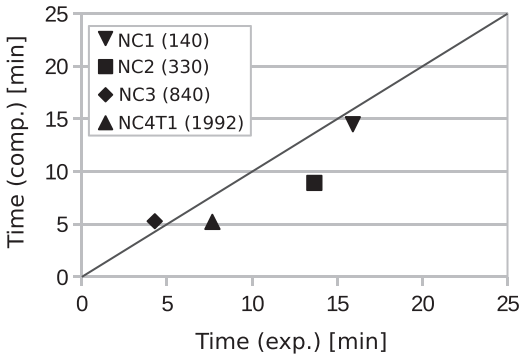

Fig. 13. Minimum required time MRT_γ.

The time MRT_A for HT1 is shown in Fig. 14. Computed results are in good agreement with the experimental ones. MRT_A decreased when graphite nodule count increased, see Fig. 14a. This behavior occurs because nucleation of ferrite platelets at graphite surface becomes more important that nucleation at tip of existing platelets, being the rate of the former bigger than the rate of the latter. MRT_A decreased when austempering temperature increased, see Fig. 14b. This behavior occurs because the nucleation rate and size of ferrite platelets increase when austempering temperature increases [20].

Fig. 15 shows the computed phase volume fractions and dimensional change, at the end of the heat treatment, for different austempering time corresponding to experiment HT2. The graphite volume fraction remained constant because the model assumes that its value is not modified during the ausferritic and martensitic transformations. The volume fraction of ferrite platelets increased when austempering time increased too, because the austempering transformation was developed for more time. When austempering time increases, more amount of carbon is rejected from ferrite to austenite. If the austenite carbon content is high enough, austenite is not consumed by martensite, i.e. all the austenite is retained at ambient temperature. This fact explains why martensite volume fraction decreased when austempering time increased. On the other hand, when austempering time increases more amount of austenite is consumed by ferrite platelets, explaining why the austenite volume fraction had a maximum when the austempering time is equal to 75 min. By means of comparison with the above mentioned experiment, it is observed that austenite volume fraction is well computed by the model when this phase is consumed by the ausferritic and martensitic transformations. Regarding the final dimensional change, positive values of this output were obtained in microstructures with a martensite volume fraction $f_m > 0.12$, while its minimum value (negative) occurred for the maximum amount of austenite. When the ausferritic transformation ended, the sample also experimented a negative dimensional change.

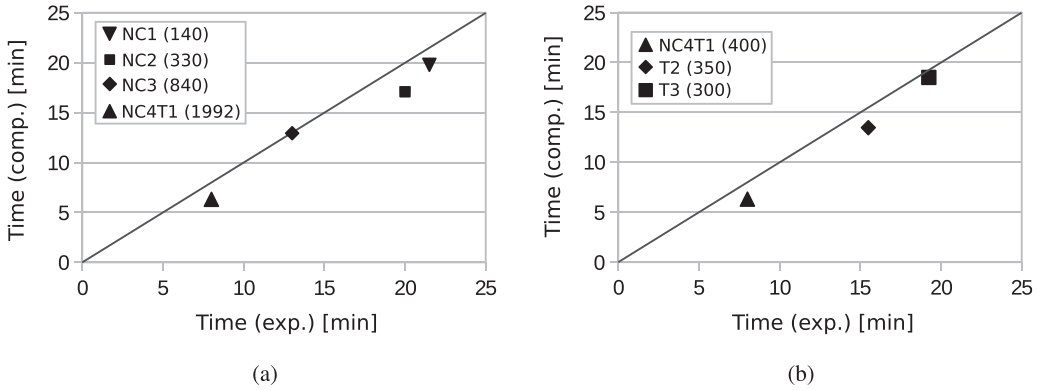

(a) (b)

Fig. 14. Minimum required time MRT_A. Influence of (a) graphite nodule count and (b) austempering temperature.

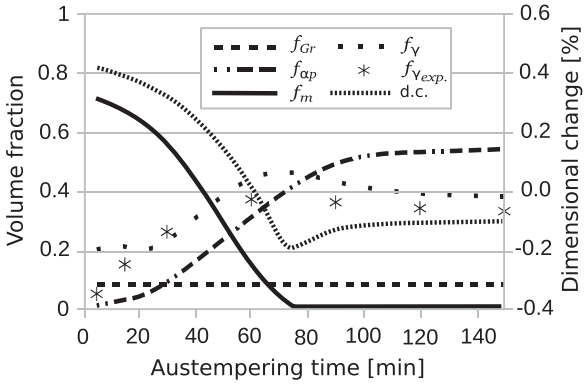

Fig. 15. Volume fraction and dimensional change at the end of the heat treatment for HT2.

5. Conclusions

The *three-step* austempering heat treatment has been modeled in several works, however seldom have thermal and mechanical phenomena been considered. For example, some microstructural features as graphite nodule count and distribution of austenite carbon content were not considered in the metallurgical model hindering their usage.

In this work a thermo-mechanical-metallurgical model has been proposed. The thermal and mechanical models are solved at the macroscale by means of the finite element method; meanwhile the metallurgical model is solved at the microscale using a representative volume element for each considered phase transformation.

The most relevant results obtained with the present model were the evolutions of temperature, dimensional change, and phase fractions through the heat treatment; also the minimum times for austenitization (MRT_γ) and austempering (MRT_A) stages were predicted. The performance of the model was tested by comparison with experimental results.

The main conclusions of the study may be summarized as follows:

1. The final microstructure is obtained as the result of the development of reverse eutectoid, ausferritic and martensitic transformations that occur in the different stages of the heat treatment.
2. The variation of graphite nodule count modifies the development of reverse eutectoid and ausferritic transformations. Its effect is observed in the minimum times for austenitization MRT_γ and austempering MRT_A stages, in which the mentioned transformations take place, respectively. An increment of graphite nodule count reduces MRT_γ and MRT_A.
3. The variation of austempering temperature modifies the development of ausferritic transformation and its effect is observed in the minimum time for the austempering stage MRT_A. An increment of austempering temperature decreases MRT_A.
4. Low values of austempering time allow to obtain a martensitic-ausferritic matrix, meanwhile high values allow to obtain a full ausferritic matrix, indicating the importance of this process parameter in the obtaining of the desired microstructure and the importance of the determination of MRT_A.
5. The maximum final dimensional change of a coupon occurs for a final matrix with a maximum amount of martensite (for an austempering time close to zero), whereas the minimum final dimensional change occurs for a final matrix with a maximum amount of austenite (for an austempering time less than MRT_A).

The model presented in this work extends the use of numerical methods in complex technological process with all the well-known advantages that this implicates. Furthermore, this model allow to (a) understand how some complex phenomena interact each other in the *three-step* austempering heat treatment, (b) design ductile iron parts to be heat treated, and (c) choose the appropriate values of the heat treatment parameters to obtain the required mechanical properties. Despite the metallurgical model represents adequately the considered phase transformations, the microsegregation of alloy elements will be included as part of future research in order to improve this model.

Acknowledgements

During the course of this research A.D. Boccardo had a postdoctoral scholarship from CONICET and P.M. Dardati was supported by a grant from Universidad Tecnológica Nacional. D.J. Celentano gratefully acknowledges the support of CONICYT through REDES Project 150041. L.A. Godoy is members of the research staff of CONICET.

References

[1] B. Bosnjak, B. Radulovic, K. Pop-Tonev, V. Asanovic, Influence of microalloying and heat treatment on the kinetics of bainitic reaction in austempered ductile iron, J. Mater. Eng. Perform. 10 (2) (2001) 203–211.
[2] U. Batra, S. Ray, S. Prabhakar, The influence of nickel and copper on the austempering of ductile iron, J. Mater. Eng. Perform. 13 (1) (2004) 64–68.
[3] D. Putman, R. Thomson, Microstructural and mechanical property modelling of austempered ductile iron, Int. J. Cast. Met. Res. 16 (2003) 191–196.
[4] M. Yescas, H. Bhadeshia, Model for the maximum fraction of retained austenite in austempered ductile cast iron, Mater. Sci. Eng. A 333 (2002) 60–66.
[5] A. Trudel, M. Gagné, Effect of composition and heat treatment parameters on the characteristics of austempered ductile irons, Can. Metall. Q. 36 (5) (1997) 289–298.
[6] U. Batra, S. Ray, S. Prabhakar, Impact properties of copper-alloyed and nickel-copper alloyed ADI, J. Mater. Eng. Perform. 16 (4) (2007) 485–489.
[7] A. Sosa, M. Echeverría, O. Moncada, Influence of nodule count on residual stresses and distortion in thin wall ductile iron plates of different matrices, J. Mater. Process. Technol. 209 (2009) 5545–5551.
[8] E. Fraś, M. Górny, E. Tyrała, H. Lopez, Effect of nodule count on austenitising and austempering kinetics of ductile iron castings and mechanical properties of thin walled iron castings, Mater. Sci. Technol. 28 (12) (2012) 1391–1396.
[9] M. Górny, E. Tyrała, H. Lopez, Effect of copper and nickel on the transformation kinetics of austempered ductile iron, J. Mater. Eng. Perform. 23 (10) (2014) 3505–3510.

[10] C. Liu, X. Xu, Z. Liu, A. FEM, modeling of quenching and tempering and its application in industrial engineering, Finite Elem. Anal. Des. 39 (2003) 1053–1070.
[11] B. Ferguson, Z. Li, A. Freborg, Modeling heat treatment of steel parts, Comput. Mater. Sci. 34 (2005) 274–281.
[12] L. Huiping, Z. Guoqun, N. Shanting, H. Chuanzhen, FEM simulation of quenching process and experimental verification of simulation results, Mater. Sci. Eng. A 452–453 (2007) 705–714.
[13] C. Şimşir, C.H. Gür, A. FEM, based framework for simulation of thermal treatments: application to steel quenching, Comput. Mater. Sci. 44 (2008) 588–600.
[14] M. Yaakoubi, M. Kchaou, F. Dammak, Simulation of the thermomechanical and metallurgical behavior of steels by using ABAQUS software, Comput. Mater. Sci. 68 (2013) 297–306.
[15] H. Qingqiang, S. Jia, Y. Chengxin, Z. Junyou, Z. Zongbo, Thermo-mechanical modeling and simulation of microstructure evolution in multi-pass H-shape rolling, Finite Elem. Anal. Des. 76 (2013) 13–20.
[16] P. Vasconcelos, A. Gießmann, J. Dias-de-Oliveira, A. Andrade-Campos, Heat treatment analysis of multiphase steels through the use of a coupled phase field and finite element model methodology, Comput. Mater. Sci. 107 (2015) 139–150.
[17] U. Batra, S. Ray, S. Prabhakar, Mathematical model for austenitization kinetics of ductile iron, J. Mater. Eng. Perform. 14 (5) (2005) 574–581.
[18] R. Thomson, J. James, D. Putman, Modelling microstructural evolution and mechanical properties of austempered ductile iron, Mater. Sci. Technol. 16 (2000) 1412–1419.
[19] W. Kapturkiewicz, A. Burbelko, J. Lelito, E. Fraś, Modelling of ausferrite growth in ADI, Int. J. Cast. Met. Res. 16 (1–3) (2003) 287–292.
[20] A. Boccardo, P. Dardati, D. Celentano, L. Godoy, A microscale model for ausferritic transformation of austempered ductile irons, Metall. Mater. Trans. A 48 (1) (2017) 524–535.
[21] W. Kapturkiewicz, E. Fraś, A.A. Burbelko, Computer simulation of the austenitizing process in cast iron with pearlitic matrix, Mater. Sci. Eng. A 413–414 (2005) 352–357.
[22] E. Hepp, V. Hurevich, W. Schäfer, Integrated modeling and heat treatment simulation of austempered ductile iron, in: Proceedings of the IOP Conference Series: Materials Science and Engineering, 33 (1), article number 012076.
[23] A. Boccardo, P. Dardati, D. Celentano, L. Godoy, M. Górny, E. Tyrała, Numerical simulation of austempering heat treatment of a ductile cast iron, Metall. Mater. Trans. B 47 (1) (2016) 566–575.
[24] G. Rees, H. Bhadeshia, Bainite transformation kinetics part 2 non-uniform distribution of carbon, Mater. Sci. Technol. 8 (1992) 994–996.
[25] L. Meier, M. Hofmann, P. Saal, W. Volk, H. Hoffmann, In-situ measurement of phase transformation kinetics in austempered ductile iron, Mater. Charact. 85 (2013) 124–133.
[26] D. Celentano, A large strain thermoviscoplastic formulation for the solidification of sg cast iron in a green sand mould, Int. J. Plast. 17 (2001) 1623–1658.
[27] D. Celentano, Thermomechanical simulation and experimental validation of wire drawing processes, Mater. Manuf. Process. 25 (7) (2010) 546–556.
[28] F. Christien, M. Telling, K. Knight, A comparison of dilatometry and in-situ neutron diffraction in tracking bulk phase transformations in a martensitic stainless steel, Mater. Charact. 82 (2013) 50–57.
[29] J. Miettinen, Calculation of solidification-related thermophysical properties for steels, Metall. Mater. Trans. B 28B (1997) 281–297.
[30] R.M. Ghergu, J. Sertucha, Y. Thebault, J. Lacaze, Critical temperature range in standard and Ni-bearing spheroidal graphite cast iron, ISIJ Int. 52 (11) (2012) 2036–2041.
[31] H. Bhadeshia, Bainite in Steels, 2nd ed., IOM Communications Ltd., London, 2001.
[32] R. Grange, H. Stewart, The temperature range of martensite formation, Trans. AIME 167 (1945) 467–494.
[33] S. Khan, H. Bhadeshia, Kinetics of martensite transformation in partially bainitic 300M steel, Mater. Sci. Eng. A A129 (1990) 257–272.
[34] D. Celentano, P. Dardati, F. Carazo, L. Godoy, Thermomechanical-microstructural modelling of nodular cast iron solidification, Mater. Sci. Technol. 29 (2) (2013) 156–164.
[35] O. Zienkiewicz, R. Taylor, The Finite Element Method, 4th Ed. Vol. 1–2, McGraw-Hill, London, 1989.
[36] J. Simo, T. Hughes, Computational Inelasticity, Vol. 7 of Interdisciplinary Applied Mathematics, Springer-Verlag, New York, 1998.
[37] A. Boccardo, Thermo-mechanical-metallurgical modelling of austempering heat treatment of ductile irons (in Spanish), Ph.D. thesis, Universidad Nacional de Córdoba, Facultad de Ciencias Exactas, Físicas y Naturales, Córdoba, Argentina, 2017. ⟨http://hdl.handle.net/11086/4758⟩.
[38] J. Lacaze, V. Gerval, Modelling of the eutectoid reaction in spheroidal graphite Fe-C-Si alloys, ISIJ Int. 38 (7) (1998) 714–722.